Eur. Phys. J. D **33**, 229–234 (2005)
DOI: 10.1140/epjd/e2005-00063-3

THE EUROPEAN PHYSICAL JOURNAL D

High electron stabilization rate in slow collisions of bare Ne^{10+} with C_{60}

J. Bernard[1,a], R. Brédy[1], L. Chen[1], S. Martin[1], A. Salmoun[2], M.-C. Buchet-Poulizac[1], and B. Wei[1,3]

[1] Laboratoire de Spectrométrie Ionique et Moléculaire[b], 43 boulevard du 11 novembre 1918, 69622 Villeurbanne Cedex, France
[2] Université Cadi Ayyad, Faculté des Sciences, Semlalia, B.P. 2390, Marrakech, Morocco
[3] Institute of Modern Physics, Chinese Academy of Sciences, Lanzhou 730000, P.R. China

Received 6 September 2004 / Received in final form 21 December 2004
Published online 3 May 2005 –

Abstract. We report cross-section measurements of collisions between bare Ne^{10+} ions and C_{60} at two different collision velocities ($v = 0.3$ and 0.64 a.u.). We focus our attention on small impact parameter collisions ($b < C_{60}$ radius), in which C_{60} can be considered as a nanometric solid target. The final charge state distribution corresponding to these small impact parameter events is modeled using a multi-cascade charge equilibration model. We show that for bare Ne^{10+} ions, the initial emptiness of the $n = 1$ shell leads to higher rates for the stabilization on the projectile of the first two electrons.

PACS. 34.70.+e Charge transfer – 34.50.Bw Energy loss and stopping power – 34.50.-s Scattering of atoms and molecules

1 Introduction

Since the first pioneering experiments of collisions between Slow Highly Charged Ions (SHCI) and C_{60} a decade ago [1], a great effort has been made to understand and model the multiple electron capture processes and the formation of hollow atoms on the projectile [2–4]. It is still a challenging task to model the subsequent decay of such highly excited exotic species. SHCI-C_{60} collisions (or other nanometric target) have many common features with SHCI-surface or SHCI-solid collisions (formation of hollow atoms, ejection of a great number of electrons, X-ray emission...). In such experiments, it has been demonstrated by measuring the energy of secondary electrons or by X-ray spectroscopy that different kinds of configurations are populated whether the projectile is above or below the surface [6–8]. As the ion approaches the surface, it is neutralized by resonant electron capture on high lying Rydberg states forming a so-called Hollow Atom of the first generation (HA1). When the projectile is to penetrate under the surface, the large-n orbitals of Rydberg electrons do not have enough space to exist anymore so that these electrons are quickly ejected and other electrons can be captured on lower-n states forming a Hollow Atom of the second generation (HA2), which is then to decay by electron (autoionization) or photon (X-rays) emission. These HA2 configurations are supposed to have many electrons in the same excited level. Vaeck et al. [9] carried out a Hartree-Fock calculation to determine statistical properties (binding energies, lifetimes...) of such exotic multi-excited configurations in some particular cases. These calculations were consistent with the experimental short lifetimes of hollow atoms observed in $Xe^{30+}-C_{60}$ collisions [10].

Studies concerning nanostructures such as clusters or C_{60} are often supported by the "bridge the gap" idea between atomic and macroscopic scale physics. Here, SHCI-C_{60} collisions provide the opportunity to induce, depending on the impact parameter, atom-like collisions (large impact parameters, number of active electrons r smaller than the initial charge q_i, no energy loss or small energy gain and small diffusion angle), surface-like collisions (impact parameters comparable to the C_{60} radius, $r \geq q_i$, small energy losses, larger diffusion angles), solid-like collisions (impact parameter smaller than the C_{60} radius, $r \geq q_i$, large energy losses — several hundreds eV —, large diffusion angles). For the $Xe^{30+}-C_{60}$ collision system, our previous work has shown that the number of active electrons can largely exceed the initial projectile charge, especially for solid-like collisions in which about 80 active electrons were observed. Considering the high initial projectile charge, and the effective thickness of the target, a simple cascade model has been derived to predict the final projectile charge state distribution. It has been shown that the projectile charge does not reach its equilibrium value like in collisions with a thick carbon target, due to the limited number of available electrons in C_{60}. In this paper, we present experimental cross-sections for the $Ne^{10+}-C_{60}$ collision system and we focus our attention

[a] e-mail: bernard@lasim.univ-lyon1.fr
[b] UMR 5579 du CNRS

mainly on solid-like collisions in order to study the evolution of the final charge state distribution as a function of the projectile velocity in the range of 0.3−0.7 a.u. For the interpretation, we follow the papers [5,10] and we show that, in spite of the rather small initial projectile charge, the same multi-cascade decay model developed in the case of Xe^{30+} allows to fit the experimental final charge state distributions.

2 Experiment

The experimental set-up has been already described in previous papers [11,12], we only recall here the main useful features and the latest evolutions. Ne^{10+} ions were produced by the SUPERSHIPIE ion source and extracted towards the LIMBE beam line of GANIL in Caen by setting the source at various voltages between 5 and 21 kV. Thus, the collision energy has been varied between 46 and 206 keV (i.e. velocities of 0.3, 0.64 a.u., respectively) taking into account a deceleration of 4 keV at the entrance of the collision region. The vacuum in the collision chamber has been maintained better than 2×10^{-9} mbars. The beam was collimated by an entrance vertical slit and a 500 μm hole separated by 0.5 m. The slit opening has been set such that no more than 10 000 collision events per second (corresponding to a few tens of pA beam intensity) could be counted in order to avoid any saturation of the detectors and double collisions. A C_{60} effusive jet is prepared by heating a C_{60} powder in an oven at about 500 °C. The diameter of the oven nozzle is 1 mm and the C_{60} jet is collimated by two holes (2 mm and 1 mm in diameter) before the collision zone. Thus the collision volume is about 0.4 mm^3 and has approximately a cylindrical shape. The scattered projectiles are charge and energy analyzed by a cylindrical electrostatic analyzer (radii: 210 and 200 mm). The recoil ions and electrons are extracted towards opposite directions by a transverse electrostatic field. This extraction field is created by applying 800 and 0 V on two parallel grids separated by 8 mm. Two sets of compensation electrodes creating electric fields in the opposite direction of the extraction field are placed on each side of the extraction electrodes in order to compensate the projectile deviation due to the extraction field. After extraction, the recoil ions are accelerated towards a 435 mm time of flight (TOF) tube. An electrostatic focusing lens and a steering system are interposed between the extraction and the TOF tube in order to optimize the collection efficiency of the recoil ions. The recoil ions are detected by a position sensitive detector composed of two Multi-Channel Plates (MCP) that create a 10^6 electron current per hitting ion and a Multi-Anode (MA). The MA, composed of 121 square pavements (3 mm^2), collects the electron currents exiting from the MCP. Each pavement is connected to its own amplification, discrimination and time measurement electronic chain. The time measurement is made independently for each pavement using four multi-channel (32 channels), multi-hit (16 hits/channel) LeCroy 3377 CAMAC device. Besides the imaging purpose, this detector allows the detection of two identical

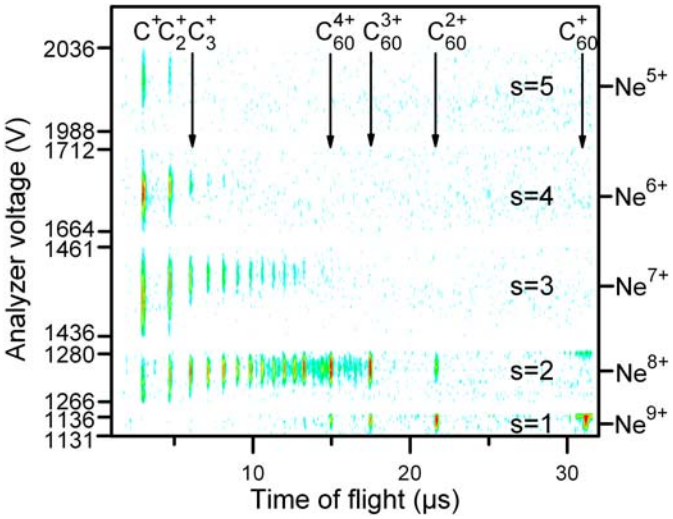

Fig. 1. Projectile–recoil ion spectrum (PR-RI). Coincidence counts are displayed in a two-dimensional spectrum. The vertical axis stands for the projectile analyzer voltage (scanned during the experiment) and the horizontal axis stands for the TOF of the recoil ions. The projectile peaks corresponding to final charges from 5 to 9 ($s = 1-5$) were successively scanned. Only rough data are shown here, i.e., no normalization have been made.

fragments (same TOF) hitting the detector at different positions without any dead time. The electrons are accelerated towards a PIPS (Passivated Implanted Planar Silicon) detector set at a 20 kV bias. The amplitude of the PIPS signal is proportional to the energy deposited by the incoming electrons, therefore it provides a measurement of the number of electrons coming out of the collision (the energy deposited by n electrons corresponds to $20n$ keV). However, in the data analysis procedure, a particular care has to be taken to include the effect of the backscattered electrons that contribute to peaks of lower energies [11,13]. All data were recorded event by event in list mode, so that different kinds of spectra can be extracted from these data for display and analysis purposes [14].

During the experiment, the projectile analyzer bias is scanned in order to integrate over the whole profile of each scattered projectile peak $Ne^{(10-s)+}$. The maximum number of stabilized electrons, s_{max}, has been found to be 6 at 46 keV and 5 for 206 keV impact energies. Figure 1 shows a typical 2-dimensional spectrum where the recoil ion TOF and the analyzer voltage are displayed on x-axis and y-axis respectively. Here only raw data are displayed, but a careful normalization is made in order to obtain the relative cross-sections σ^s. Due to completely different cross-sections as a function of s, different beam intensities are needed for scanning from Ne^{9+} to Ne^{5+}. With increasing beam intensities, we scanned first the Ne^{9+} and Ne^{8+} ($s = 1$ and 2) peaks together then the Ne^{8+} to Ne^{6+} ($s = 2$ to 4) peaks together and finally the Ne^{6+} and Ne^{5+} ($s = 4$ and 5) peaks together. Then we normalized all peaks to the same beam intensity. From the horizontal projection on the analyzer voltage axis in Figure 1, we obtain the profiles of the scattered projectile peaks. As an example,

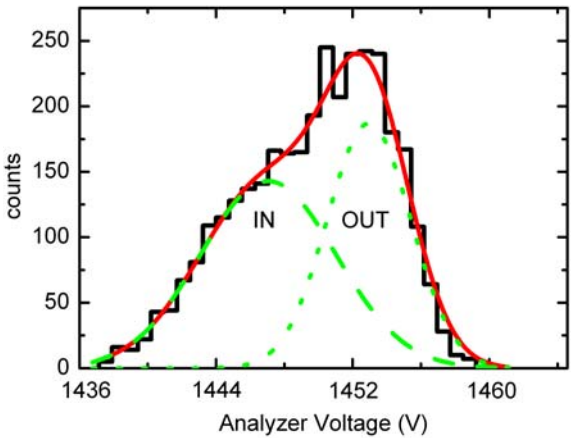

Fig. 2. Histogram: partial projection (from Fig. 1) of Ne^{7+} ($s = 3$) scattered projectiles peak. This projection is fitted by two Gaussian curves corresponding to IN (dashed curve) and OUT (dotted curve) contributions. The plain curve is the sum of the IN and OUT curves.

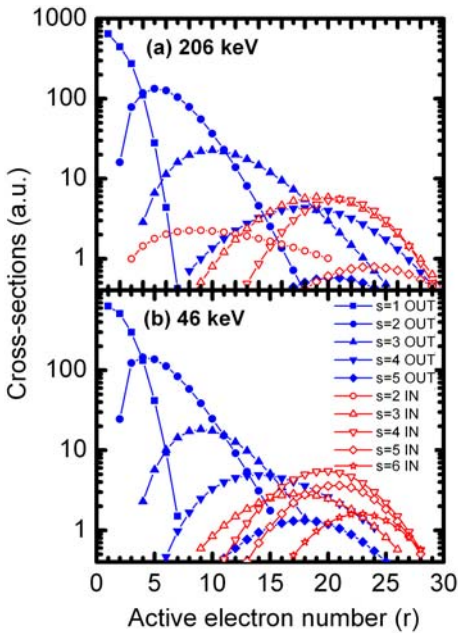

Fig. 3. Partial cross-sections σ_r^s of $Ne^{10+}-C_{60}$ collisions for projectile velocities of 0.64 a.u. (a) and 0.3 a.u. (b). Lines are to guide the eye.

Figure 2 shows the projectile peak profile for $s = 3$. This profile can be clearly fitted by 2 Gaussian curves, the high voltage one corresponding to OUT collisions (impact parameter $b >$ C_{60} radius), the energy loss or gain of which is considered negligible, and the low voltage one is attributed to IN collisions ($b <$ C_{60} radius). The shift of the IN peak respectively to the OUT peak corresponds after calibration of the analyzer to an energy loss of 950 eV for the IN collisions. The error bar on this value is estimated to 150 eV. The analysis of these profiles, i.e. the deconvolution method to extract IN and OUT contributions and to convert them to IN and OUT cross-sections using electron spectra has been fully described in previous papers [12,14].

3 Results and discussion

Figure 3 displays partial cross-sections σ_r^s corresponding to the stabilization on the projectile of s electrons from r active electrons, while $n = r - s$ of them are ejected to the continuum during (fast processes) or after the collision (slow autoionization processes). Black marks correspond to OUT collisions and open marks to IN collisions. As previously observed with Ne^{10+} at 100 keV collision energy [12], an $s = 2$ IN contribution can be observed for 206 keV, however no evidence of such $s = 2$ IN contribution has been observed for 46 keV. The relative contributions to the total cross-section are found to be 89%, 6%, 5% for atom-like, surface-like and solid-like collisions, respectively. These values are almost independent of the projectile velocity in the energy range considered here. It strengthens the purely geometrical attributions to atom-, surface- or solid-like collisions. Atom-like collisions can be modeled classically by employing the over-barrier model combined (OBM) with a statistical energy distribution model (SED) as shown in previous papers [12,15]. This kind of purely static model is not suited to represent any velocity dependence of the collision cross-section. For atom-like collisions however, only a very small velocity dependence is observed and the calculations of our previous paper on Ne^{10+} at 100 keV are still applicable here.

In this paper, we want to focus our attention on solid-like collisions, especially on the final charge state distributions and their velocity dependence. From Figure 3, we extract the final charge state distributions for the frontal solid-like collisions corresponding to velocities of 0.30 and 0.64 a.u., and from paper [12] we obtain the final charge state distribution for 0.44 a.u. These three distributions are displayed in Figures 4a and 5a. From these distributions, we determine the mean exit charge shown in Figure 6. Figure 6 shows also the experimental mean exit charge we obtained for 0.51 and 0.56 a.u. velocities. Error bars of ± 0.5 are estimated from the statistic standard deviation on particle counting. Figure 6 exhibits an overall increase of the mean exit charge with the velocity that corresponds to the clear shift of the final charge state distribution towards higher charges in Figure 3b.

A complete model describing these solid-like collisions would include the treatment of electron capture processes to determine the configurations that are likely to be populated and the knowledge of all atomic data needed to estimate the autoionizing (and, eventually, radiative) lifetimes of these configurations. None of these are currently available apart from the calculations of Vaeck et al. [9] concerning some hollow configurations of xenon and nitrogen. First, we follow the reasoning of paper [5] that concerns slow highly charged ions colliding on amorphous thin carbon foils. It is assumed there that the deexcitation of the second generation hollow atoms inside the target follows an exponential decay law from the initial charge q_i

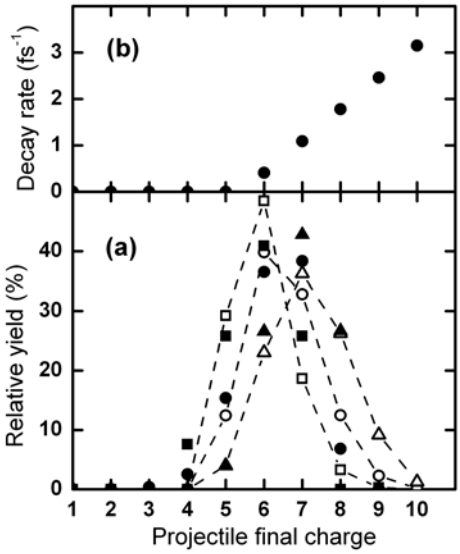

Fig. 4. (a) Experimental (black symbols) and calculated (open symbols) projectile final charge state distributions for $v = 0.3$ a.u. (squares), $v = 0.44$ a.u. (circles) and $v = 0.64$ a.u. (triangles). (b) Decay rate constants α_q resulting from the fitting procedure assuming a linear increase of α_q with q. Lines in (a) are to guide the eye.

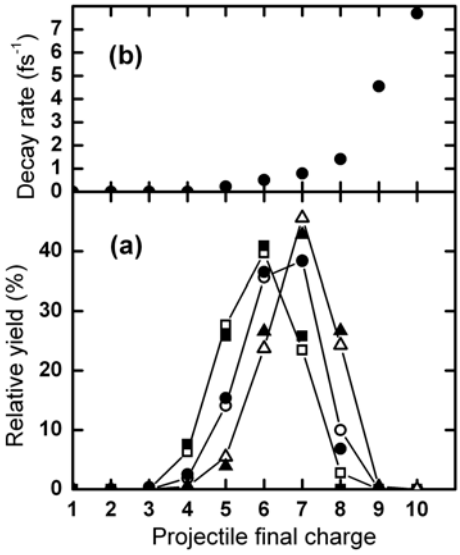

Fig. 5. Same as Figure 4 but decay rate constants α_q are assumed to follow two different linear scaling laws (see text).

to the equilibrium charge in the solid q_{eq}. A value of q_{eq} of about 1 is obtained from the Bohr stripping criterion: $q_{eq} = vZ^{1/3}$ where the velocity v is given in atomic units. The decay to the equilibrium charge is given by:

$$q(x) = q_{eq} + (q_i - q_{eq})e^{-\alpha(x/v)} \tag{1}$$

where α is the mean decay rate constant, q_i is the initial charge (here $q_i = 10$), x is the interaction length. Now, the symbol q denotes the core charge of the projectile. In the fitting procedure the product αx is considered as an adjustable parameter. In Figure 6, the dashed curve

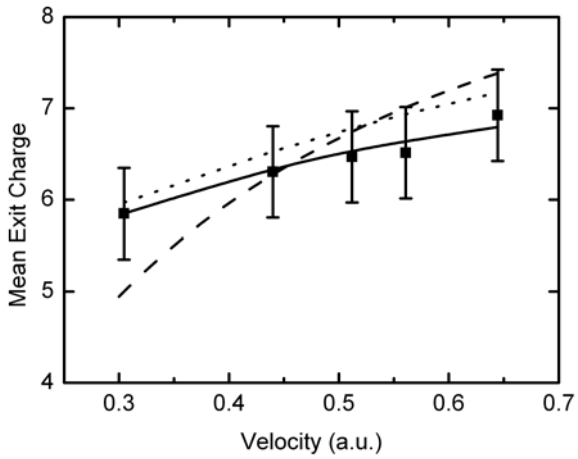

Fig. 6. Squares: experimental mean exit charge for inside cage collisions of Ne^{10+} with C_{60} as a function of the projectile velocity. Dashed curve: model using equation (1). Dotted curve: multi-cascade model using a linear function for the time constants α_q. Plain curve: same as the dotted curve with the decay rates α_q assumed to follow two different linear scaling laws.

is the best fit to experimental data using equation (1) and the parameter $\alpha x = 0.23$ a.u. In order to estimate the interaction length, it can be considered that the HA2 is formed when the projectile is completely neutralized. From the OBM, we calculate the distance at which the 10th electron is captured $R_{10} = 18.5$ a.u. and we estimate the interaction length to be $x = 2R_{10} = 37$ a.u. Thus we find $\alpha = 4 \times 10^{14}$ s^{-1} for the decay rate constant. This value is consistent with those obtained in papers [5,10]. Although the agreement with the experimental mean exit charge is rather good according to the errors bars, this model doesn't allow to determine theoretical final charge state distributions.

A multi-cascade model is now presented following papers [10,16] in order to estimate the population on final charge q of the scattered projectiles. The population on core charge q at a given time t is assumed to be governed by the following set of coupled differential equations:

$$\begin{cases} \dfrac{dN_{10}}{dt} = -\alpha_{10}N_{10} & \text{for} \quad q = 10 \\ \dfrac{dN_q}{dt} = \alpha_{q+1}N_{q+1} - \alpha_q N_q & \text{for} \quad q < 10 \end{cases} . \tag{2}$$

The solution functions of this system are given by:

$$N_q(t) = N_0 \left(\prod_{p=0}^{q-1} \alpha_p \right) \sum_{p=0}^{q} \frac{\exp(-\alpha_p t)}{\prod\limits_{\substack{m=0 \\ m \neq p}}^{p} (\alpha_m - \alpha_q)} \tag{3}$$

where the α_q is the mean decay rate that includes the effects of all transitions occurring while an ion of core charge q decays to the core charge $(q-1)$; t is the interaction time obtained as above from $2R_{10}/v$. Since the decay rates α_q are not accessible by any calculation at the present time, they are treated as adjustable parameters. However, as already stated in [10], it is reasonable to

consider that α_q is given by an increasing function of q. Indeed, like in ion-solid collisions, the projectile charge should tend to an equilibrium charge and the decay should be faster as the projectile charge is far from this equilibrium charge. The first guess and simplest function is a linear function:

$$\alpha_q = \gamma_a (q - q_a) \quad (4)$$

for $q \geq q_a$ and $\alpha_q = 0$ otherwise. q_a corresponds to the minimum exit charge of the projectile, i.e., this is the critical charge under which the population is zero. This leaves only two adjustable parameters for the fitting process (γ_a and q_a). The theoretical final projectile charge state distributions are displayed in Figure 4a for comparison with experiment and Figure 4b shows the corresponding values of α_q. The centers and widths of the final charge state distributions are rather well reproduced by the model. The best agreement is found for $\gamma_a = 7.0 \times 10^{14}$ s^{-1} and $q_a = 5.4$. γ_a is found slightly larger for Ne^{10+} than for Xe^{30+} (3.7×10^{14} s^{-1}) but in the same order of magnitude. Time constants in the order of magnitude of a few femtoseconds are consistent with the Hartree-Fock calculation of papers [9,17] for nitrogen and xenon hollow configurations. However, slight discrepancies between experiment and model can be noted. For instance, the experimental limit charge has been found to be 4, slightly smaller than the adjusted value (5.4). This limit charge can be estimated via a simple energy criterion: an electron can be transferred from the charged C_{60} to the projectile only if the projectile ionization potential (Ip) is larger than the target one. Figure 3 shows that for $s = 6$ (final charge $q = 4$), the mean number of active electrons is about 23, leading to $Ip(C_{60}^{23+}) \approx 73.3$ eV to be compared with $Ip(Ne^{4+}) = 93.3$ eV. On the other hand, for the final charge $q = 3$ ($s = 7$), we have $Ip(Ne^{3+}) = 63.46$ eV only. So, it is expected, and experimentally confirmed, that the projectile cannot exit the collision with a final charge $q = 3$ and that the limit charge is 4. Moreover, we found remarkable that if we increase the values for α_{10} and α_9, the general agreement between theoretical and experimental distributions is much better. Consequently, the above rough linear approximation has to be improved. We introduce a second linear function $\alpha_q = \gamma_b (q - q_b)$ with $\gamma_b > \gamma_a$ and $q_b > q_a$. In other words, for each value of q (from 0 to 10), α_q is given by the maximum of $\{0; \alpha_q = \gamma_a (q - q_a); \alpha_q = \gamma_b (q - q_b)\}$. We have now four adjustable parameters: γ_a, γ_b, q_a, and q_b. The resulting fit is displayed in Figure 5a with corresponding α_q values in Figure 5b. The adjusted values are $\gamma_a = 2.8 \times 10^{14}$ s^{-1} (very close to the Xe^{30+} value), $\gamma_b = 3.1 \times 10^{15}$ s^{-1}, $q_a = 4.2$ (in good agreement with the value obtained via the energy criterion) and $q_b = 7.6$. In Figure 6, it can be also noted that the agreement of the calculated mean exit charge with the experiment is much improved with the present multi-cascade model (plain curve). Other test functions have been tried for α_q and only the best agreement between experimental and theoretical final charge state distributions are shown here. Although the choice of two linear functions may appear somewhat fortuitous, the agreement between theory and experiment is always improved when a discontinuity is introduced in the α_q function to increase the α_9 and α_{10} values.

For Xe^{30+} ions, only one linear constraint function for α_q has been necessary since, in that case, the first electrons are stabilized into the quasi-equivalent states of the $n = 3$ shell. For Ne^{10+} ions, the discontinuity of α_q shows that shell effects are more important for bare ions due to the stabilization of the two first electrons in the $n = 1$ shell lying far below the $n = 2$ shell. The high stabilization rates α_{10} and α_9 show that the lifetime of an ion with one or two holes in the $n = 1$ shell is very short. The initially empty $n = 1$ shell of the projectile implies that a greater number of autoionization steps are necessary to stabilize the two first electrons on this shell. Considering electron stabilization as a sequential process, among all decay time constants $\tau_q (= \alpha_q^{-1})$, τ_{10} is the shortest ($\sim$0.13 fs) but it corresponds to the largest number of autoionization cascades in order to fill the $n = 1$ shell. Consequently, the lifetime of each intermediate state of the cascade should be even shorter than τ_{10} and also shorter than autoionization lifetimes for the filling of the $n = 2$ shell. Nevertheless, with hollow atoms, one should also consider "shake-off" processes that involve the perturbation of spectator electrons and could result in fast supplementary electron ejection.

4 Conclusion

Cross-sections have been measured for $Ne^{10+}-C_{60}$ collisions at various impact energies in the range 46−206 keV. The projectile energy loss measurement has been used to extract the inside cage contribution of the cross-sections and subsequently, the final projectile charge state distributions for those frontal collisions. Theoretical final charge state distributions were calculated using the same decay model as for Xe^{30+}. The good overall agreement shows that the model is applicable to a wide range of projectiles, even when the initial projectile charge is rather small. However, we have shown that for the bare Ne^{10+}, it is necessary to employ a different constraint function for the core charge decay rates α_{10} and α_9 in order to take into account the fast stabilization process of the two first electrons in the $n = 1$ shell.

The experiments were performed at LIMBE (GANIL, Caen). The authors are much grateful to L. Maunoury and J.-Y. Paquet for preparing high quality ion beams.

References

1. B. Walch, C.L. Cocke, R. Voelpel, E. Salzborn, Phys. Rev. Lett. **72**, 1439 (1994)
2. A. Langereis, J. Jensen, A. Fardi, K. Haghighat, H.T. Schmidt, S.H. Schwartz, H. Zettergren, H. Cederquist, Phys. Rev. A **63**, 062725 (2001)
3. H. Zettergren, H.T. Schmidt, H. Cederquist, J. Jensen, S. Tomita, P. Hvelplund, H. Lebius, B. Huber, Phys. Rev. A **66**, 032710 (2002)

4. U. Thumm, J. Phys. B **28**, 91 (1995)
5. M. Hattass, T. Schenkel, A.V. Hamza, A.V. Barnes, M.W. Newman, J.W. MacDonald, T.R. Niedermayr, G.A. Machicoane, D.H. Schneider, Phys. Rev. Lett. **82**, 4795 (1999)
6. A. Arnau, F. Aumayr, P.M. Echenique, M. Grether, W. Heiland, J. Limburg, R. Morgenstern, P. Roncin, S. Schippers, R. Schuch, N. Stolterfoht, P. Varga, T.J.M. Zouros, H.P. Winters, Surf. Sci. Rep. **27**, 117 (1997)
7. J.P. Briand, G. Giardino, G. Borsoni, M. Froment, M. Eddrief, C. Sébenne, S. Bardin, D. Schneider, J. Jin, H. Khemliche, Z. Xie, M. Prior, Phys. Rev. A **54**, 4136 (1996)
8. J.P. Briand, S. Thuriez, G. Giardino, G. Borsoni, M. Froment, M. Eddrief, C. Sébenne, Phys. Rev. Lett. **77**, 1452 (1996)
9. N. Vaeck, N.J. Kylstra, Phys. Rev. A **65**, 062502 (2002)
10. S. Martin, R. Brédy, J. Bernard, J. Désesquelles, L. Chen, Phys. Rev. Lett. **89**, 183401 (2002)
11. J. Bernard, R. Brédy, S. Martin, L. Chen, J. Désesquelles, M.-C. Buchet-Poulizac, Phys. Rev. A **66**, 013209 (2002)
12. S. Martin, L. Chen, R. Brédy, J. Bernard, A. Salmoun, B. Wei, Phys. Rev. A **69**, 043202 (2004)
13. F. Aumayr, G. Lakits, H. Winter, Appl. Surf. Sci. **47**, 139 (1991)
14. S. Martin, J. Bernard, L. Chen, A. Denis, J. Désesquelles, Eur. Phys. J. D **12**, 27 (2000)
15. J. Bernard, R. Brédy, L. Chen, S. Martin, A. Salmoun, Phys. Rev. A **68**, 53223 (2003)
16. S.M. Younger, W.L. Wiese, Phys. Rev. A **17**, 1944 (1978)
17. P. Palmeri, P. Quinet, N. Zitane, N. Vaeck, J. Phys. B **34**, 4125 (2001)